applied optics

Single-pulse ablation of multi-depth structures via spatially filtered binary intensity masks

Daniel J. Heath,* James A. Grant-Jacob, Robert W. Eason, and Ben Mills

Optoelectronics Research Centre, University of Southampton, Southampton SO17 1BJ, UK
**Corresponding author: djh2v07@soton.ac.uk*

Received 21 September 2017; revised 31 October 2017; accepted 31 October 2017; posted 12 January 2018 (Doc. ID 307609); published 8 March 2018

Digital micromirror devices (DMDs) show great promise for use as intensity spatial light modulators. When used in conjunction with pulsed lasers of a timescale below the DMD pixel switching time, DMDs are generally only used as binary intensity masks (i.e., "on" or "off" intensity for each mask pixel). In this work, we show that by exploiting the numerical aperture of an optical system during the design of binary masks, near-continuous intensity control can be accessed, whilst still maintaining high-precision laser-machining resolution. Complex features with ablation depths up to ∼60 nm, corresponding to grayscale values in bitmap images, are produced in single pulses via ablation with 150 fs laser pulses on nickel substrates, with lateral resolutions of ∼2.5 μm.

OCIS codes: (140.3300) Laser beam shaping; (230.6120) Spatial light modulators; (220.4000) Microstructure fabrication; (220.1140) Alignment; (220.2560) Propagating methods.
https://doi.org/10.1364/AO.57.001904

1. INTRODUCTION

Modification of the laser spatial intensity profile is a key enabling technology for applications ranging from laser machining [1–6] to imaging [7–9], as it allows the output intensity profile of a laser beam to be optimized for a particular application. Laser beam shaping approaches may be characterized as static [10] (e.g., a fixed mask, aperture, or beam homogenizer) or dynamic [e.g., via the use of liquid crystal spatial light modulators (LC SLMs) [11–14] and digital micromirror devices (DMDs) [4,6,15–19]]. LC SLMs offer the advantage of continuous intensity and/or phase control for repetition rates up to ∼1 kHz. DMDs, while operating at considerably higher repetition rates of up to ∼30 kHz, only offer binary intensity control (i.e., the intensity for each pixel is either "on" or "off"), which may be a severe limitation for some applications. Therefore, there is a particular interest in adapting this technology for continuous intensity control. While previous work has demonstrated micromachining techniques using DMDs as grayscale exposure masks [20–22], the grayscale was only possible through the rapid dithering of DMD pixels over a long exposure time (typically tens of seconds), which averaged to grayscale values during the exposures from cw sources. This technique is not suitable for single submicrosecond pulses, which are below the switching time of DMD pixels. The approach discussed here is for adapting a DMD-based beam shaping setup into one that offers continuous intensity control ("grayscale") for use in high-precision femtosecond laser machining, but this technique should prove equally applicable to other beam shaping applications.

We have already shown the use of DMDs for control of the spatial intensity profile for single-pulse high-precision laser machining in materials traditionally difficult to process [6], over large (∼1 cm^2) areas [15], and at subdiffraction-limit resolution [18]. Here we show the circumvention of the apparent binary mask limitation of DMDs and demonstrate continuous intensity control via the ablation of multi-depth structures in nickel using single exposures from these binary masks.

Previous studies have focused on digital holographic techniques for laser beam shaping that employ DMDs [12,23], though these have focused on the generation of binary intensity patterns. While some degree of intensity control via DMDs has been shown [24], the resulting projected patterns remained binary, and the method was not applicable to complex grayscale patterns. The generation of high-order spatial modes has been demonstrated with the use of DMDs [25], and the capability to produce more general intensity distributions is expected to be highly relevant to this field. This work demonstrates an algorithm for the generation of binary intensity masks, which, when projected through an optical system, result in grayscale intensity patterns at the image position. The intensity patterns have been shown to ablate multi-depth structures in single 150 fs exposures, with lateral resolutions as low as ∼2.5 μm.

The concept of continuous intensity control is discussed in Section 2, the experimental setup in Section 3, experimental results and analysis in Section 4, and conclusions in Section 5.

2. BINARY MASK MULTI-LEVEL INTENSITY CONTROL

When imaging a binary intensity mask, there will be unavoidable loss of resolution as a result of the limited numerical aperture (NA) of the optical system, typically removing spatial frequency components in a light pattern above a certain value, which is a well-known phenomenon and is commonly referred to as spatial filtering. In practice, this can be produced either deliberately or unintentionally via the finite diameter of any optical element, such as a lens, aperture, or entrance pupil to a microscope objective. Any binary intensity mask at the object plane will undergo a convolution with the point-spread function (PSF), such that the complex light field from nearby pixels in a DMD mask, for instance, will overlap and interfere at the image plane. Work by others has exploited the PSF of DMD pixels to build up microlens arrays [26] with the same periodicity as the DMD mirror array. While this effect determines a resolution limit reproducible in an optical system at a given wavelength, it will also be shown to allow the generation of grayscale patterns at the image plane from a binary mask.

An important consideration is that the intensity value at the imaging plane depends on both the ratio of pixels "on" to "off" as well as the particular arrangement of those pixels, as each arrangement will result in a different distribution of spatial frequency intensities and hence change the total intensity propagating through the spatial filter. A simplistic, and intuitive (though ultimately incorrect), method to achieve 50% intensity at the sample within a given region would be to switch 50% of the pixels off. In a block of 10×10 pixels, for example, the specific 50 pixels that are chosen to be "on" may cause the intensity to deviate from the desired 50% value. If the 50 pixels are in single pixel-wide, straight, alternating lines, i.e., every other column of pixels within the 10×10 block, there will be a different intensity value compared to the case where the 50 pixels were arranged in a single line of 5×10 pixels. This is because the multiple thin lines in the first example will require a greater proportion of high spatial frequencies than the single wide line; when high spatial frequencies are removed due to spatial filtering, more energy remains therefore as in the second example.

To correct for this uncertainty in the selection of pixels to remain "on" for a desired intensity distribution, we designed an algorithm that iterates between the object and image plane whilst taking into account the specific degree of spatial filtering introduced into the experimental setup by the NA of the microscope objective used, which generates a mask pattern that produces an intensity profile at the sample that more closely matches the one that is desired. The algorithm is a preprocessing step that requires no real-time experimental feedback. The steps of the algorithm are as follows:

(1) Define a target grayscale pattern, i.e., the desired intensity distribution at the imaging plane, and use this to define an ideal field by taking the square root of target values (as intensity is proportional to the absolute value of the field squared). This ideal field is the first iteration of what shall be referred to as the *current field*.

(2) Generate an initial mask intensity distribution by turning on mirrors with probability defined by their grayscale value on the interval [0,1], i.e., a pixel with value of 0.5 in the target pattern will have a 50% chance of being "on" in the initial mask. In practice, all values in the mask are generated in parallel by comparing a 2D array of ideal field values to a random matrix of numbers, both in the interval [0,1].

(3) Simulate the propagation of the pattern from the mask plane to the imaging plane, taking into account the spatial filtering. This is achieved by taking the Fourier transform of the mask, retaining only spatial frequencies below a certain value (as defined by the NA of the optical system), and then taking the inverse Fourier transform. This is referred to as the current field profile.

(4) Calculate the difference between the ideal field profile at the sample and the current field profile. This difference is referred as the "error field."

(5) Propagate the error field from the imaging plane to the object plane and back to the imaging plane, taking into account the spatial filtering.

(6) Add a fraction (0.05 used here) of the spatially filtered error field, to the current field profile, and take the absolute value.

(7) Compare this absolute field to the same random matrix as used in step 2 to generate the next iteration of the binary mask. Check whether the algorithm has reached its end criteria (in this case, 100 iterations, where little improvement was seen beyond 20 iterations); if not, repeat from step 3.

To demonstrate the importance of the algorithmic correction described here, Fig. 1 simulates an ideal grayscale checkerboard pattern that is made of 0%, 50%, and 100% intensities, with a range of binary mask patterns, along with their simulated spatially filtered intensity profiles. To simulate the spatial filtering, the mask patterns defined on 1024×1024 arrays were Fourier transformed to the spatial frequency domain and then multiplied by a circular aperture function (2D array, value 1 within a central circle, value 0 otherwise) of a radius of 81 pixels, whose size was determined to correspond to the NA of our system (0.42). The filtered field was then inverse Fourier transformed, and the absolute square values were taken to simulate final intensity patterns.

There are three approaches for generating the mask pattern, namely, (a) ordered, i.e., a regular on/off pattern of pixels in regions where 50% intensity is desired, (b) a random selection of 50% of pixels switched off in regions where 50% intensity is desired, and (c) generated via our iterative algorithm. Part (d) of Fig. 1 shows the result that could be produced using a mask that allows continuous intensity control, which is not possible to display on a DMD. For the approaches (a) and (b), 50% of the pixels are "on" in the desired 50% intensity region. For (c), the number of pixels may not be exactly 50%, due to the applied corrections. Whilst all three mask patterns look similar, the difference resulting from spatial filtering is clear in the final intensity profiles. In the cases of (a) and (b), there is considerable deviation from the ideal intensity value within the

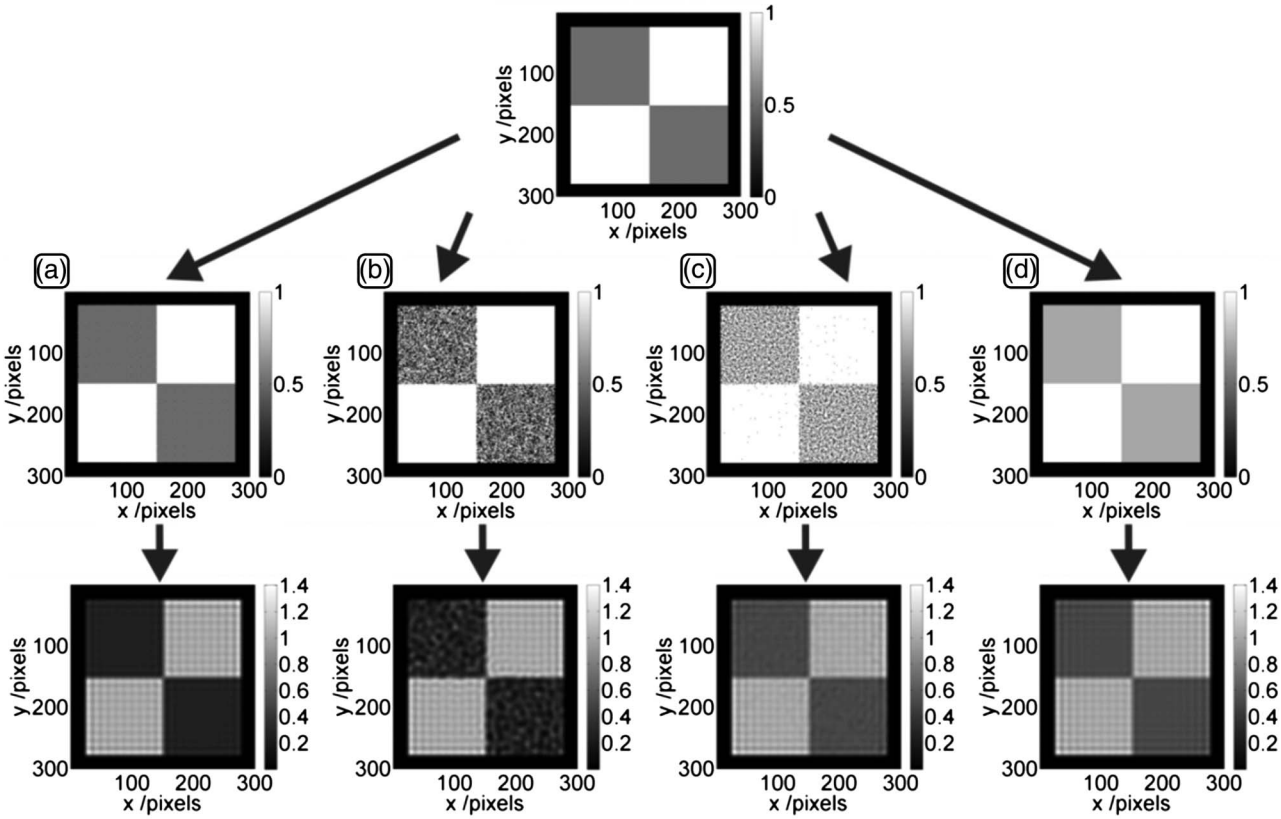

Fig. 1. Target intensity pattern is a 2 × 2 checkerboard with two diagonally opposite squares at half the intensity of the remaining two. Different binary masks are used to attempt to recreate this distribution. The effect of spatial filtering is shown for (a) an ordered mask, i.e., every other pixel "on" in greyscale region, (b) a random mask, (c) the algorithmic approach presented here, and (d) a mask with continuous intensity control.

Table 1. Mean and Standard Deviation Values of Points Within the Intended 50% Intensity Regions from the Projected Intensity Patterns in Fig. 1

	Mean Intensity Value (Arb Units)	Standard Deviation/Mean Value
Fig. 1(a)	0.2523	0.1914
Fig. 1(b)	0.2575	0.3379
Fig. 1(c)	0.4965	0.1307
Fig. 1(d)	0.4953	0.1314

50% regions. For (c), the deviation is considerably smaller. This comparison is illustrated via the mean and standard deviation (as a fraction of the mean) values across regions intended to be at 50% intensity in Table 1.

The values of ∼0.25 in parts (a) and (b) demonstrate the importance of spatial filtering on the final intensity; though 50% of pixels are "on," a high proportion of the energy is lost when high spatial frequencies are removed. Part (d) shows that even a continuous intensity mask, without algorithmic corrections, is no better than the iteratively generated mask from (c). For larger aperture sizes, the algorithm was in fact observed to produce higher fidelity final recreations of the intended intensity distribution than grayscale masks with continuous intensity control and no corrections.

3. EXPERIMENTAL SETUP

In this work, the binary mask is a digital micromirror device. DMDs consist of an array of approximately 1000 by 1000 mirrors, each of size ∼10 μm (the actual number and size of mirrors depends on the specific model), where each mirror can be independently rotated on a diagonal axis to −12 deg or +12 deg, with respect to the DMD surface. For incoherent beams, this process can be used to selectively reflect regions of an incident beam into two beam paths, typically one for imaging and the other into a beam dump. For coherent beams, the nature of the 2D array of mirrors results in a far-field 2D array of interference peaks being produced, where each interference peak contains spatial information corresponding to the entire DMD pattern. The intensity of each interference peak is determined by the underlying intensity envelope. In the case of a coherent beam, the mirrors do not switch the direction of the reflected light but rather change the angle of the underlying intensity envelope. Hence, when a single interference peak is imaged onto a sample, the spatial intensity profile on the sample can correspond to the digital pattern displayed on the DMD (i.e., the arrangement of +12 deg/−12 deg mirrors).

The experimental setup is shown in Fig. 2. Laser pulses (∼150 fs) at 800 nm central wavelength, with pulse energy up to 1 mJ were spatially homogenized via a Pi-Shaper

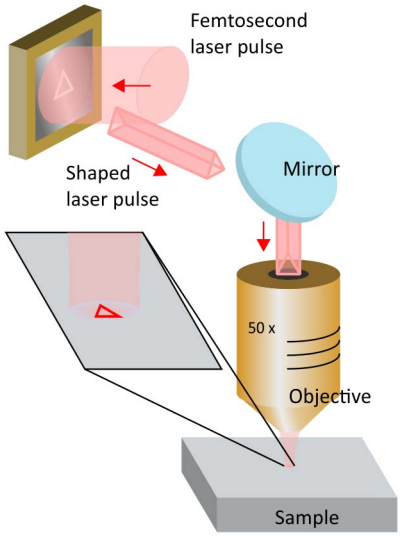

Fig. 2. Experimental schematic showing the use of a DMD as a binary spatial light modulator.

(PI 6_6) into a top-hat intensity profile, which then illuminated the DMD (DLP 3000, Texas Instruments). The pattern loaded onto the DMD (the *mask pattern*), shown as a triangle in the figure, was then projected as an intensity profile through a microscope objective onto the sample, where it would ablate the target material. The exact spatial filtering was calculated using the NA of the objective in combination with scanning electron microscope measurements from previous ablation experiments of the geometric scaling of DMD pixel size to the projected intensity pattern lateral size [18].

4. EXPERIMENTAL RESULTS

In order to demonstrate the application of the algorithmic correction to laser machining, Figs. 3(a)–3(d) show interferometrically measured (Zygo Zescope, accurate to 0.1 nm depth measurements) depth profile results of structures ablated in electroless nickel. Figure 3(a) shows results from the random selection method of generating grayscale masks shown in Fig. 1(b), while Figs. 3(b)–3(d) show results generated via the iterative algorithm presented in Section 2. Inclusion of the result from ablation using the mask generated via random selection served to demonstrate the superiority of the algorithm—as expected, a high proportion of energy was lost in high spatial frequencies at the point of filtering, and hence little ablation was observed in the "gray" regions. Indeed, to observe any ablation in these regions at all, a much higher fluence of 2.42 mJ/cm^2 was required, as compared to the ∼1 mJ/cm^2 used for the other exposures, and the depth modulation in those regions was much less homogenous. The corresponding high intensity in the "all on" regions of Fig. 3(a) then resulted in damage to the remaining substrate

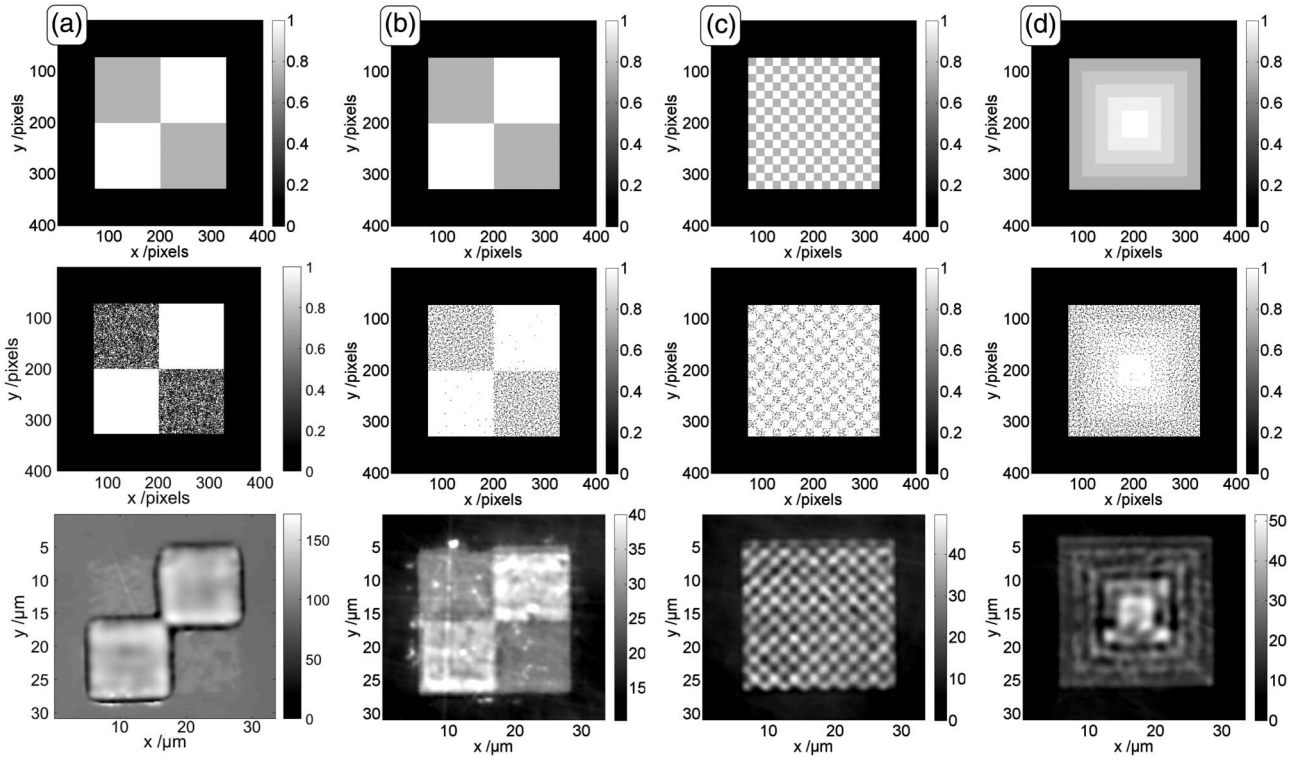

Fig. 3. Selection of masks and corresponding ablated structures, showing (top row) the intended intensity pattern, (middle row) the binary mask as displayed on the DMD, and (bottom row) the resulting interferometrically measured depth profiles of ablated structures in electroless nickel. Part (a) was generated using the random selection method shown in Fig. 1(b), while (b)–(d) were generated using the algorithm described in Section 2. Each structure was machined in a single laser pulse. In (a), the mask was generated using the random selection method shown in Fig. 1(b) and exposed at a fluence of 2.42 mJ/cm^2. In (b), the DMD was exposed at a fluence of 0.62 mJ/cm^2, in (c) at 0.88 mJ/cm^2, and in (d) at 1.41 mJ/cm^2. The color map in the top row represents intended intensity, while in the bottom row it represents depth of ablation in nanometers.

in the form of a raised lip of material around their edges. The intended spatial intensity profiles are shown, as well as the binary masks generated via the algorithm, which were displayed during a single 150 fs exposure to produce each structure. Electroless nickel, an amorphous metal, was chosen to eliminate possible grain boundary effects. Note that the three structures were produced using different incident fluences at the DMD to achieve similar peak ablation depths, as each desired pattern contained a different proportion of high spatial frequencies.

Figures 3(a) and 3(b) show simple checkerboard structures similar to that shown in Fig. 1, demonstrating that two-level ablation in a single pulse was achieved and comparing the results achieved via the random selection method in Fig. 1(b) to the algorithmic approach; the random selection method was chosen for comparison as it was more applicable to arbitrary grayscale patterns than the ordered method in Fig. 1(a). Figure 3(b) then demonstrates the apparent limit of lateral resolution for the technique, at ∼2.5 μm (close to the limit found for the setup previously when projecting binary patterns [15]). Figure 3(c) then shows a stepped square pyramid structure with five distinct depths of ablation.

Further to the step-like structure in Fig. 3(c), which shows multiple depths ablated in a single pulse, the flexibility of this algorithm is demonstrated in Fig. 4, where a grayscale photograph of one of the authors [Fig. 4(a)] is converted into a binary mask [Fig. 4(b)] and the interferometrically measured depth profile after a single pulse ablation of the nickel substrate [Fig. 4(c)]. While results in Fig. 3 show that high resolution and multi-stepped structures are possible, the structure in Fig. 4 demonstrates that a near-continuous distribution of depth machining is possible, with a combination of step-like and smooth changes. Some trade-off in terms of resolution is evident, and, in particular, the uniform background level of the original image has not been perfectly reproduced. This error could likely be corrected by the addition of real-time feedback to the technique; rather than assuming an ideal circular top-hat illumination of the DMD, a live-camera view of the DMD surface would enable exact illumination quality input to the algorithm, which would result in more faithful recreation of the target pattern.

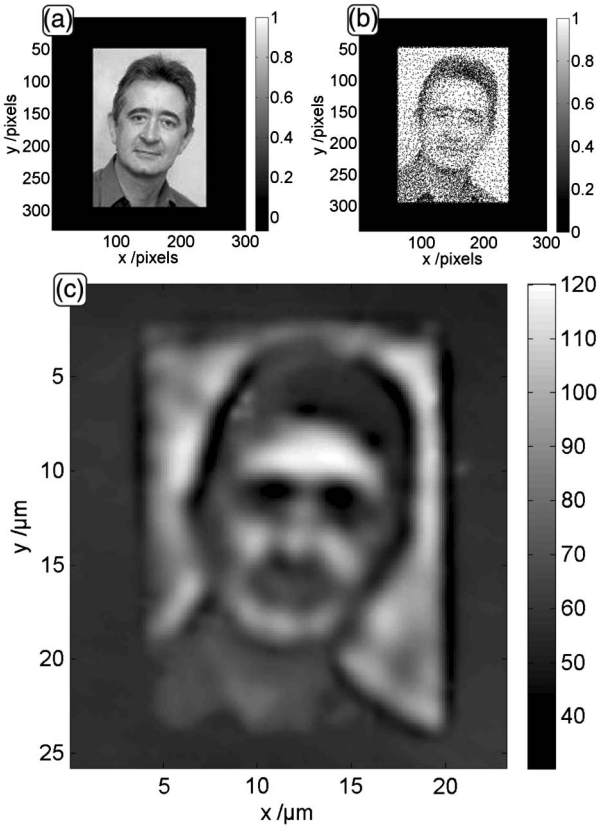

Fig. 4. Image of one of the authors, ablated into electroless nickel in a single femtosecond pulse with a fluence of 1.41 mJ/cm^2 at the DMD. (a) The original image with the color map relating to intensity, (b) the binary mask displayed on the DMD, and (c) the interferometrically measured depth profile in electroless nickel with the color map in nanometers.

As observed in Fig. 4(c), the depth of machining is up to ∼60 nm. While the color map in Fig. 4(c) shows a range of 120 nm for the ablation depth, it must be noted that this is due to the formation of ∼60 nm high structures formed above the substrate background height, which is a typical effect at border regions when laser machining with high fluences.

5. CONCLUSIONS

An algorithm has been presented for the generation of binary masks that project to grayscale intensity patterns after the spatial filtering inherent to the majority of optical systems. A DMD has been used to display the masks during exposure of 150 fs laser pulses, which were then imaged onto electroless nickel and caused ablation. The different grayscale values of the desired intensity distributions were shown to be reproduced in the interferometrically measured depth profiles of the resulting structures. Resolutions as low as 2.5 μm were observed, with depth modulation up to 60 nm in a single exposure.

Funding. Engineering and Physical Sciences Research Council (EPSRC) (EP/L022230/1, EP/N03368X/1, EP/N509747/1).

Acknowledgment. The data for this work is accessible through the University of Southampton Institutional Research Repository DOI:10.5258/SOTON/D0253.

REFERENCES

1. L. Kelemen, S. Valkai, and P. Ormos, "Parallel photopolymerisation with complex light patterns generated by diffractive optical elements," Opt. Express **15**, 14488–14497 (2007).
2. C. Sun, N. Fang, D. M. Wu, and X. Zhang, "Projection micro-stereolithography using digital micro-mirror dynamic mask," Sens. Actuators A Phys. **121**, 113–120 (2005).
3. Z. Kuang, D. Liu, W. Perrie, S. Edwardson, M. Sharp, E. Fearon, G. Dearden, and K. Watkins, "Fast parallel diffractive multi-beam femtosecond laser surface micro-structuring," Appl. Surf. Sci. **255**, 6582–6588 (2009).
4. R. C. Y. Auyeung, H. Kim, S. Mathews, and A. Piqué, "Spatially modulated laser pulses for printing electronics," Appl. Opt. **54**, F70–F77 (2015).
5. Y. Lu, G. Mapili, G. Suhali, S. Chen, and K. Roy, "A digital micro-mirror device-based system for the microfabrication of complex, spatially

patterned tissue engineering scaffolds," J. Biomed. Mater. Res. A **77**, 396–405 (2006).
6. B. Mills, D. J. Heath, M. Feinaeugle, J. A. Grant-Jacob, and R. W. Eason, "Laser ablation via programmable image projection for submicron dimension machining in diamond," J. Laser Appl. **26**, 041501 (2014).
7. C. M. Watts, D. Shrekenhamer, J. Montoya, G. Lipworth, J. Hunt, T. Sleasman, S. Krishna, D. R. Smith, and W. J. Padilla, "Terahertz compressive imaging with metamaterial spatial light modulators," Nat. Photonics **8**, 605–609 (2014).
8. M. F. Duarte, M. A. Davenport, D. Takhar, J. N. Laska, T. Sun, K. F. Kelly, and R. G. Baraniuk, "Single-pixel imaging via compressive sampling," IEEE Signal Process. Mag. **25**, 83–91 (2008).
9. B. Sun, M. P. Edgar, R. Bowman, L. E. Vittert, S. Welsh, A. Bowman, and M. J. Padgett, "3D computational imaging with single-pixel detectors," Science **340**, 844–847 (2013).
10. L. Rapp, C. Constantinescu, Y. Larmande, A. P. Alloncle, and P. Delaporte, "Smart beam shaping for the deposition of solid polymeric material by laser forward transfer," Appl. Phys. A **117**, 333–339 (2014).
11. K. R. Kim, J. Yi, S. H. Cho, N. H. Kang, M. W. Cho, B. S. Shin, and B. Choi, "SLM-based maskless lithography for TFT-LCD," Appl. Surf. Sci. **255**, 7835–7840 (2009).
12. M. Sakakura, N. Fukua, Y. Shimotsuma, K. Hirao, and K. Miura, "Hologram design for holographic laser machining inside transparent materials," Proc. SPIE **8607**, 86070V (2013).
13. R. J. Beck, J. P. Parry, W. N. MacPherson, A. Waddie, N. J. Weston, J. D. Shephard, and D. P. Hand, "Application of cooled spatial light modulator for high power nanosecond laser micromachining," Opt. Express **18**, 17059–17065 (2010).
14. R. D. Simmonds, P. S. Salter, A. Jesacher, and M. J. Booth, "Three dimensional laser microfabrication in diamond using a dual adaptive optics system," Opt. Express **19**, 24122–24128 (2011).
15. D. J. Heath, B. Mills, M. Feinaeugle, and R. W. Eason, "Rapid bespoke laser ablation of variable period grating structures using a digital micromirror device for multi-colored surface images," Appl. Opt. **54**, 4984–4988 (2015).
16. M. Feinaeugle, D. J. Heath, B. Mills, J. A. Grant-Jacob, G. Z. Mashanovich, and R. W. Eason, "Laser-induced backward transfer of nanoimprinted polymer elements," Appl. Phys. A **122**, 398–402 (2016).
17. D. J. Heath, M. Feinaeugle, J. A. Grant-Jacob, B. Mills, and R. W. Eason, "Dynamic spatial pulse shaping via a digital micromirror device for patterned laser-induced forward transfer of solid polymer films," Opt. Mater. Express **5**, 1129–1136 (2015).
18. D. J. Heath, "Sub-diffraction limit laser ablation via multiple exposures using a digital micromirror device," Appl. Opt. **56**, 6398–6404 (2017).
19. Y. X. Ren, R. De, Lu, and L. Gong, "Tailoring light with a digital micromirror device," Ann. Phys. **527**, 447–470 (2015).
20. X. Ma, Y. Kato, F. Kempen, Y. Hirai, T. Tsuchiya, F. Keulen, and O. Tabata, "Multiple patterning with process optimization method for maskless DMD-based grayscale lithography," Procedia Eng. **120**, 1091–1094 (2015).
21. M. Zhang, Q. Deng, L. Shi, A. Cao, H. Pang, and S. Hu, "A gray matching method for cylindrical lens array fabrication based on DMD lithography," Manip. Manuf. Meas. Nanoscale **127**, 145–147 (2016).
22. W. Iwasaki, T. Takeshita, Y. Peng, H. Ogino, H. Shibata, Y. Kudo, R. Maeda, and R. Sawada, "Maskless lithographic fine patterning on deeply etched or slanted surfaces, and grayscale lithography, using newly developed digital mirror device lithography equipment," Jpn. J. Appl. Phys. **51**, 06FB05 (2012).
23. J. Cheng, C. Gu, D. Zhang, and S.-C. Chen, "High-speed femtosecond laser beam shaping based on binary holography using a digital micromirror device," Opt. Lett. **40**, 4875–4878 (2015).
24. R. C. Y. Auyeung, H. Kim, S. Mathews, and A. Piqué, "Laser forward transfer using structured light," Opt. Express **23**, 422–430 (2015).
25. Y. X. Ren, Z. X. Fang, L. Gong, K. Huang, Y. Chen, and R. DeLu, "Dynamic generation of Ince-Gaussian modes with a digital micromirror device," J. Appl. Phys. **117**, 133106 (2015).
26. X.-Y. Ding, Y.-X. Ren, L. Gong, Z.-X. Fang, and R.-D. Lu, "Microscopic lithography with pixelate diffraction of a digital micro-mirror device for micro-lens fabrication," Appl. Opt. **53**, 5307 (2014).